REGULAR PAPER

Air-Jet Levitation of Continuum Robots: Stable Head Floating by Passive Thrust Vectoring for Enhancing Mobility

Yuichi Ambe[1] · Shuta Kamio[2] · Yu Yamauchi[3] · Masashi Konyo[2] · Kenjiro Tadakuma[4] · Shigenao Maruyama[5] · Satoshi Tadokoro[2]

Abstract

Flexible, continuum-type robots can access narrow spaces in debris areas during search-and-rescue missions. However, their current problem is the lifting capability of the head, which is necessary to surmount the rubble. This study proposes a passive-thrust vectoring method to stabilize head levitation for air-jet-actuated, long, continuum robots, and thus enhance their step-climbing abilities. An air jet can generate a thrust force that is sufficient for head levitation. A critical issue in levitation involves the backward bending of the head without using any air-jet control; however, thrust control is inappropriate because of the delay caused by the long channel. Therefore, the proposed method maintains the thrust direction constant. Sufficient conditions for global stability are derived and confirmed via dynamic simulations. The proposed method is simple and can be mechanically realized with a passive head-bending mechanism, thus contributing to a lightweight design. Experiments demonstrated that the developed air-floating-type, 7-m long robot, can achieve stabilized head levitation, and that the robot can climb a step with a height of 250 mm. Robot demonstrations in rubble justify the robot's capacity to surmount the rubble. This passive-thrust vectoring method is expected to contribute to the future enhancement of the mobility of continuum robots owing to its simplicity and practicality.

The provided video shows the head bending motion without the proposed controller, the stabilized head levitation with the proposed passive mechanism, one example of the step-climbing experiments (explained in Section 6), and demonstrations associated with Section 7.

✉ Yuichi Ambe
ambe.yuichi.es@osaka-u.ac.jp

1   Graduate School of Engineering Science, Osaka University, Toyonaka 560-8531, Osaka, Japan

2   Graduate School of Information Sciences, Tohoku University, Sendai 980-8579, Miyagi, Japan

3   Graduate School of Systems Science and Technology, Akita Prefectural University, Yurihonjo 015-0055, Akita, Japan

4   Tough Cyberphysical AI Research Center, Tohoku University, Sendai 980-8579, Miyagi, Japan

5   New Industry Creation Hatchery Center, Tohoku University, Sendai 980-8579, Miyagi, Japan

1 Introduction

Serpentine robots can access narrow spaces in debris areas during search-and-rescue missions [1, 2]. The primary roles of these robots are to move in deeper regions within debris and gather information based on observations. Conventional serpentine robots are categorized into rigid-link and flexible continuum types.

Rigid-link-type robots have rigid links and are actuated by active joints driven by motors. Hirose et al. developed an active cord mechanism (ACM) series [3, 4], which initially used passive wheels on rigid links. Active wheels [5, 6] and crawler tracks [7, 8] have been developed to improve mobility. No-wheel-type, snake-like robots were developed [9–12]. Although rigid-link-type robots exhibit good maneuverability and sensing capability characteristics, their heavy and relatively complex structures can cause several issues. For example, the tether used to provide power and

communication often gets stuck in the rubble. Furthermore, a heavy body can cause unexpected debris falls.

The flexible-continuum type has a simple, long, and lightweight structure comprising soft materials. Several studies have reported disaster response methods. For example, Tukagoshi et al. [13] developed a soft tube-type robot that thrusted into rubble by expanding its tip and pressurized an inverted, thin-walled vessel. Hawkes et al. [14, 15] proposed a similar concept and demonstrated its ability to simulate debris. Takahashi et al. [16] presented a similar approach, which used an incompressible liquid to realize an unsealed structure. In a previous study, we proposed an active-scope camera (ASC) as a self-propelled robotic video scope that allowed the insertion of a long flexible cable into narrow spaces [17, 18]. The ASC was driven by a ciliary vibration mechanism [19] that generated a thrust force by vibrating a long flexible cable covered with inclined elastic cilia. ASCs have been employed in several disaster sites [20].

The current problem with flexible, continuum-type robots is the lifting capability of the head. Head levitation is necessary to surmount the rubble. For example, when wooden buildings collapse during earthquakes, the first floors often collapse partially and empty spaces are formed wherein victims may be trapped [21]. However, these fields are surrounded by debris, such as wooden blocks and household goods. When a conventional ASC is inserted into collapsed buildings, head collisions with these obstacles often limit the available routes [20]. However, it is difficult for a long and flexible robot to climb obstacles owing to its soft body. Although a conventional ASC can bend the head using pneumatic actuators, the head often topples to the side when it tries to elevate. This is different from the motions of rigid-link-type snake robots, which can statically elevate their heads because their bodies are sufficiently rigid to support the posture [5, 12, 22].

We have proposed the use of air-jet actuation to elevate the head of a flexible, continuum robot to overcome this problem [23–25]. The robot generates an air jet from its head to generate a reaction force. This reaction force elevates the head of the ASC to surmount the rubble and allows the robot to look around its environment from a higher elevation. We also demonstrated the robot's high-mobility level over rubble [24]. However, in the previously conducted studies [23–25], we did not discuss the method or mechanism used to levitate the head in a stable manner or the basic mobility performance because we mainly focused on the robot's potential in search-and-rescue tasks.

This study proposes a method to levitate the head in a stable manner. Levitation can be realized with a lightweight passive mechanism (Fig. 1) and evaluates the step-climbing ability. The primary challenge in designing a method to achieve the aforementioned aims pertains to the fact that the head bends backward and loses control (without the need of the control of the air jet) (see Supplementary video). However, thrust control of the air jet is inappropriate because of the delay between the valve input and nozzle output caused by the long channel in the continuum robot. Thus, in this study, we propose the use of a simple, open-loop controller to maintain a constant air-jet direction instead of controlling its strength to stabilize head levitation. The analysis with the use of a dynamic model shows that the controller ensures global stability in certain conditions, which are fulfilled in numerical simulations. Subsequently, we propose a passive head-bending mechanism to realize the controller and verify stable head levitation with a robot. This approach enabled us to realize a simple and lightweight head structure. Finally,

Fig. 1 Overview of air-floating-type, active-scope camera: System overview (A), developed robot (B), and schematic showing the structure of the camera's head (C)
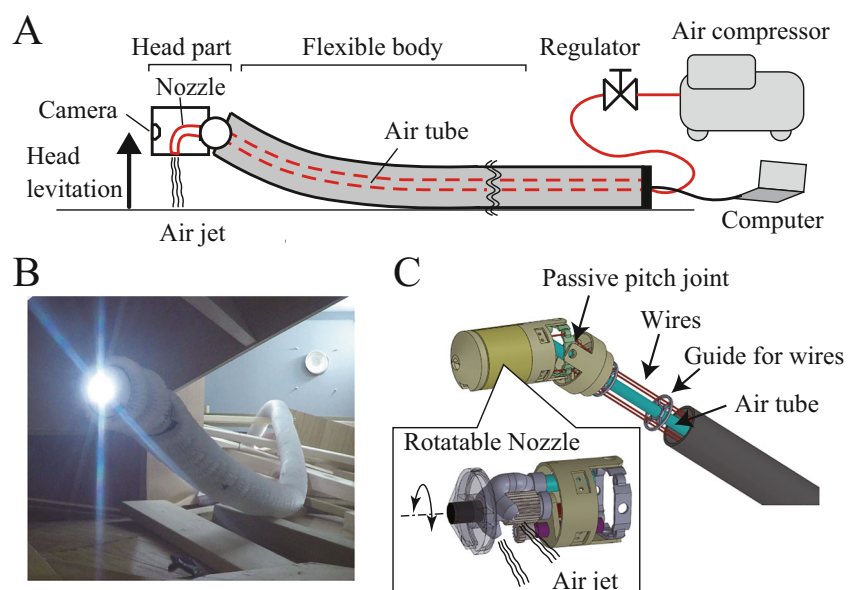
we evaluate the basic mobility performance in terms of step climbing and demonstrate the robot's mobility response on rubble.

The contributions of this study are as follows:

1. We propose an air-jet direction controller to stabilize the head levitation for a long continuum robot, which can be realized using a passive head-bending mechanism (passive thrust vectoring).
2. We integrate the controller with the ASC. We realize stable head levitation and step climbing at a height of 250 mm, which had not been achieved with a previous robot [18].

2 Related Studies

2.1 Head-Actuation Mechanisms of Continuum Robots

Many methods have been proposed to control the tip of a flexible continuum robot with a fixed root, as reviewed in [26]. Most actuation mechanisms apply a force (or torque) along the body, such as the wire-driven robots [27, 28], pneumatic-actuation robots [29, 30], and concentric tube designs [31]. In addition, some studies focus on the head control of flexible manipulators, which consist of flexible links and actuated joints [32], including the immersed situation in fluid [33].

In contrast to these robots, fluid jet actuation can generate a translational force, which is not affected by the body shape or environment in any direction. Thus, the jet-type robot can generate a levitating force against gravity regardless of its shape; this could be a significant advantage in elevating the head. However, the stabilized controller is needed, as discussed in the Introduction.

2.2 Continuum Robots Actuated by Jets

Jet-actuated continuum robots have attracted attention because of their promising features. Rico et al. [34] proposed a long, flexible robot actuated by water jets on the head. They demonstrated that the robot could move forward with water jets and elevate its head by manually controlling the water-jet-induced reaction force. Campisano et al. [35, 36] proposed a hydrojet endoscopic platform actuated by water jets to minimize the cost of gastric cancer screening exams. However, to our knowledge, no study has proposed (to-this-date) a method to achieve stable levitation.

In our previous study, we proposed the concept of an aerial, hose-type robot for firefighting using a water jet [37–41] and realized stable levitation for lengths up to 4 m. A similar concept was proposed [42, 43] according to the types of controlled multiple jet thrusts for stabilized levitation. Although we proposed the controller for stable flights in our previous study [37], this controls the direction and magnitude of the net force using multiple jet nozzles. In addition, we have not proved the stability of the controller.

In this study, we propose a controller that only uses the direction of the fluid jet, and can be installed with a simple passive mechanism. This passive thrust vectoring method has major advantages in making lightweight and thin structures, which is important to access narrow spaces. In addition, we derive a sufficient condition for the global stability of the controller for the first time.

3 Overview of the Robotic System

The developed continuum robot (air-floating-type ASC) comprises a head with a camera and nozzle, and a long flexible body (approximately equal to 7 m) covered with backward inclined cilia (Fig. 1). Owing to the cilia-driving mechanism [19], the body part can generate a forward propulsive force. Specifically, by vibrating the body with actuators, the cilia repeat the stick-and-slip motion on the ground, and the robot experiences a propelling force. The robot moved forward at a speed of approximately 100 mm/s on a wooden plate. As the cilia can generate a forward propulsive force on all the parts of the robot which touch the ground, it is possible to reach deep into the rubble without considerable slack in the body.

The structure of the head is illustrated in Fig. 1C. The head has a nozzle, and its inlet is connected to a flexible air tube inside the body. The compressor delivered compressed air through the regulator and air tube to the nozzle. The nozzle accelerated the air to emit a high-speed air jet. By expelling the air jet, a net thrust (momentum and pressure thrusts) was applied to the nozzle outlet, similar to a rocket. The regulator could adjust the air pressure to control thrust force. We installed a motor to rotate the nozzle along its longitudinal axis and steer the robot. The robot's moving functions and control frameworks are also summarized in Fig. 9 in Section 6.

The robot had a passive joint between its head and body. In addition, multiple wires were connected to constrain the head posture (Fig. 1C). These are for the stabilized levitation, and the details are presented in Sections 4 and 5.

4 Direction Controller for Stabilized Levitation

4.1 Simple Model and Equation of Motion

The physical model of the front part (Fig. 2) was designed subject to the following assumptions based on the actual robot.

Fig. 2 Model of air-floating-type active-scope camera (ASC) on the sagittal plane
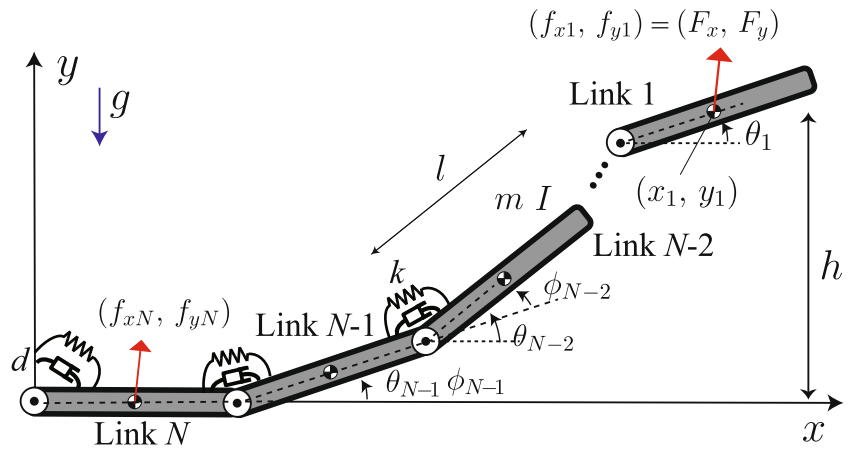
(A1) We considered only the movement of the head part (approximately 1 m from the head) of the robot because the air injection elevated only the front part. Furthermore, the root of the model was fixed at the origin to ignore the effect of the body because the robot body moved slowly in debris areas (100 mm/s) and could be twisted to a desired posture. *(A2)* We considered a model on the sagittal plane because the backward bending of the head occurred on the sagittal plane and the air jet was mainly directed downward during the climbing of a step. *(A3)* Based on [44], we approximated the continuum body as multiple rigid links connected by elastic joints and dampers. Each link i was modeled as a rigid body (mass m_i, inertia I_i, and length l), and each joint i had a rotational spring with a damper (spring stiffness k and damper coefficient $d > 0$). Furthermore, the links, except for head link 1, were uniform ($m_i = m > 0$, $I_i = I > 0$ if $i \neq 1$). *(A4)* The ground was modeled as a frictionless horizontal surface ($y = 0$) in a simple scenario. Furthermore, the normal reaction from the ground was modeled as a force applied to the center of masses (COMs) of the contact links. *(A5)* A nozzle outlet was installed on the head. We modeled the force induced by the air jet as an external force (F_x, F_y) applied to the COM of link 1. This is the control input. The force applied to the links by the pressure and momentum of the internal flow was ignored.

Based on these assumptions, the model comprised N rigid bodies. For link i, we denote the pitch angle by θ_i (generalized coordinates in this model), joint angle by ϕ_i, COM position by (x_i, y_i), and external force on the COM by (f_{xi}, f_{yi}). The link 1 denotes the head. Herein, we describe a vector with N elements as $\boldsymbol{a} = [a_1\, a_2\, \ldots\, a_N]^T$.

We derived the equation of motion with reference to [45]. The kinetic energy T can be written as

$$T = \frac{1}{2}\left(\dot{\boldsymbol{x}}^T M \dot{\boldsymbol{x}} + \dot{\boldsymbol{y}}^T M \dot{\boldsymbol{y}} + \dot{\boldsymbol{\theta}}^T J \dot{\boldsymbol{\theta}}\right), \tag{1}$$

where $\dot{\boldsymbol{x}} = -lAS_\theta\dot{\boldsymbol{\theta}}$, $\dot{\boldsymbol{y}} = lAC_\theta\dot{\boldsymbol{\theta}}$, $M = \mathrm{diag}(\boldsymbol{m})$, $J = \mathrm{diag}(\boldsymbol{I})$ $S_\theta = \mathrm{diag}(\sin\theta_1, \ldots, \sin\theta_N)$, $C_\theta = \mathrm{diag}(\cos\theta_1, \ldots, \cos\theta_N)$,

$$A = \begin{bmatrix} 1/2 & 1 & \cdots & 1 \\ 0 & 1/2 & \cdots & 1 \\ \vdots & \vdots & \ddots & \vdots \\ 0 & 0 & \cdots & 1/2 \end{bmatrix}.$$

The potential energy V can be written as

$$V = \frac{1}{2}k\boldsymbol{\theta}^T R^T R\boldsymbol{\theta} + lg\boldsymbol{m}^T A \sin\boldsymbol{\theta}, \tag{2}$$

where $\sin\boldsymbol{\theta} = [\sin\theta_1 \cdots \sin\theta_N]^T$, and R denotes an $N \times N$ matrix that satisfies $\boldsymbol{\phi} = R\boldsymbol{\theta}$. Subsequently, the Lagrangian $L = T - V$ can be derived. The dissipation function can be described as

$$U = \frac{1}{2}d\dot{\boldsymbol{\phi}}^T\dot{\boldsymbol{\phi}} = \frac{1}{2}d\dot{\boldsymbol{\theta}}^T R^T R\dot{\boldsymbol{\theta}}. \tag{3}$$

The virtual work δW performed by the external force $\boldsymbol{f}_x$, $\boldsymbol{f}_y$ can be described using the virtual displacement $\delta\boldsymbol{\theta}$ as

$$\delta W = -l\boldsymbol{f}_x^T AS_\theta\delta\boldsymbol{\theta} + l\boldsymbol{f}_y^T AC_\theta\delta\boldsymbol{\theta}. \tag{4}$$

The Euler–Lagrange equation can be written as

$$\frac{d}{dt}\frac{\partial L}{\partial\dot{\boldsymbol{\theta}}} - \frac{\partial L}{\partial\boldsymbol{\theta}} + \frac{\partial U}{\partial\dot{\boldsymbol{\theta}}} = -l\boldsymbol{f}_x^T AS_\theta + l\boldsymbol{f}_y^T AC_\theta. \tag{5}$$

By solving Eq. 5, the equation of motion can be derived as

$$H\ddot{\boldsymbol{\theta}} + D\dot{\boldsymbol{\theta}} + kR^T R\boldsymbol{\theta} + dR^T R\dot{\boldsymbol{\theta}} + lgC_\theta A^T\boldsymbol{m}$$
$$= -lS_\theta A^T\boldsymbol{f}_x + lC_\theta A^T\boldsymbol{f}_y, \tag{6}$$

where

$$H = S_\theta \overline{M} S_\theta + C_\theta \overline{M} C_\theta + J,$$
$$D = ml^2 \left(S_\theta A^T A C_\theta - C_\theta A^T A S_\theta \right) \text{diag}(\dot{\boldsymbol{\theta}})$$

$\overline{M} = l^2 A^T M A$. H denotes a positive definite matrix, and $\boldsymbol{f}_x$, $\boldsymbol{f}_y$ are determined by the control input (F_x, F_y) and normal reaction g_i as

$$f_{xi} = \begin{cases} 0 & i \neq 1 \\ F_x & i = 1 \end{cases}, \quad f_{yi} = \begin{cases} g_i & i \neq 1 \\ F_y + g_i & i = 1 \end{cases}, \quad (7)$$

$$g_i = \begin{cases} 0 & y_i > 0 \\ -k_g y_i - d_g \dot{y}_i & y_i \leq 0 \end{cases}. \quad (8)$$

The surface was modeled with a spring k_g and damper d_g, whose stiffness was sufficiently high to ignore the displacement.

4.2 Proposed Controller

The use of the thrust magnitude as a control input requires a sophisticated controller because of the time delay between the regulator's input and thrust magnitude (an approximate delay of 0.5 s for a 10 m tube with an inner diameter of 6.5 mm). Therefore, this study proposes a thrust-vectoring control method that controls the direction of the air jet. A very simple thrust vectoring control is given by

$$\vec{F} \equiv [F_x \ F_y]^T = \text{const}, \quad (9)$$

where $F_x \geq 0$ for forward movements, and $F_y \geq 0$ for head elevations. A constant force direction was maintained with respect to the inertial coordinate, whereas the magnitude of the force vector was kept constant.

This controller can be easily implemented with a passive mechanism without delay and can reduce the number of sensors and actuators (Section 5). Furthermore, this force input has a physically good feature, that is, it is a conservative force. This feature ensures that energy, including the potential function of the force, is dissipated by the innate damping elements of the robot, which becomes a candidate for the Lyapunov function, as discussed in the following section.

4.3 Theoretical Equilibrium Points and their Stability

4.3.1 Assumption to Analyze Equilibrium Points and Stability

For the analytical description, we investigated the equilibrium points and their stability in the case in which all N

links were in the air. It is difficult to investigate the equilibrium points and stability of the entire system Eq. 6 because it is a hybrid dynamical system. However, the equilibrium points can be investigated by considering only the links in the air if the ground is sufficiently stiff ($lk_g/mg \gg 0$). Because the force is applied to the head (link 1), links 1, 2, .., N_{air} are in the air in static equilibrium conditions, where N_{air} denotes the number of links in the air. Thus, if the ground is sufficiently stiff, the state variables of link i on the ground can be written as $\theta_i = \dot{\theta}_i = 0$, and the equilibrium points can be investigated using only the links in the air. If we ignore the dynamics of the links on the ground, stability can be evaluated using the N_{air} link model.

4.3.2 Equilibrium Points

The equilibrium points of this system, $(\hat{\boldsymbol{\theta}}, \dot{\hat{\boldsymbol{\theta}}} = \boldsymbol{0})$, satisfy

$$lg\boldsymbol{m}^T AC_{\hat{\theta}} + k\hat{\boldsymbol{\theta}}^T R^T R + l\boldsymbol{F}_x^T AS_{\hat{\theta}} - l\boldsymbol{F}_y^T AC_{\hat{\theta}} = \boldsymbol{0},$$

where $\boldsymbol{F}_x = [F_x \ 0 \ \cdots \ 0]^T$, $\boldsymbol{F}_y = [F_y \ 0 \ \cdots \ 0]^T$. Thus, the following N equations are derived.

$$d_i \sin(\hat{\theta}_i + \psi_i) + c_i(\hat{\boldsymbol{\theta}}) = 0, \ i \in [1, \ N], \quad (10)$$

where $d_i = \sqrt{a_i^2 + b_i^2}$, $\psi_i \in [-\pi/2, \pi/2]$, which fulfils $\sin \psi_i = a_i/d_i$, $\cos \psi_i = b_i/d_i$. $\boldsymbol{a} = lgA^T\boldsymbol{m} - lA^T \boldsymbol{F}_y$, $\boldsymbol{b} = lA^T \boldsymbol{F}_x$, $\boldsymbol{c}(\hat{\boldsymbol{\theta}}) = kR^T R\hat{\boldsymbol{\theta}}$. These equations are transcendental equations and their solutions cannot be derived analytically.

4.3.3 Stability

As a candidate for the Lyapunov function, we define

$$E'(\boldsymbol{\theta}, \dot{\boldsymbol{\theta}}) = T(\boldsymbol{\theta}, \dot{\boldsymbol{\theta}}) + V'(\boldsymbol{\theta}) - V'(\hat{\boldsymbol{\theta}}). \quad (11)$$

where

$$V'(\boldsymbol{\theta}) = V(\boldsymbol{\theta}) + V_w(\boldsymbol{\theta}), \quad (12)$$
$$V_w(\boldsymbol{\theta}) = l\boldsymbol{F}_x^T A \cos \boldsymbol{\theta} - l\boldsymbol{F}_y^T A \sin \boldsymbol{\theta}$$

The right-hand side of the equation of motion Eq. 6 can be represented as $-(\partial V_w/\partial \boldsymbol{\theta})^T$ because the control input $\vec{F}$ is a conservative force. Furthermore, E' denotes the total energy of the system if we consider that V_w is the potential energy. Subsequently, the following equation was derived,

$$\frac{dE'}{dt} = -2U \leq 0, \quad (13)$$

where equality is attained if and only if $\dot{\boldsymbol{\theta}} = \boldsymbol{0}$; thus, energy decreases monotonically over time.

In addition, the sufficient condition for the function E' to be positive definite ($E' \geq 0$, where equality is attained if and only if $\dot{\boldsymbol{\theta}} = \boldsymbol{0}, \boldsymbol{\theta} = \hat{\boldsymbol{\theta}}$) can be written using Theorem 2 in the Appendix.

$$kR^T R - 2SD_d > 0, \tag{14}$$

where $S = \text{diag}(s_i),\ D_d = \text{diag}(d_i)$,

$$s_i = \begin{cases} \dfrac{1}{2}|\sin(\hat{\theta}_i + \psi_i)|, & \cos(\hat{\theta}_i + \psi_i) \geq 0 \\ \dfrac{1}{2}, & \cos(\hat{\theta}_i + \psi_i) < 0 \end{cases}, \tag{15}$$

where the inequality of Eq. 14 shows that $kR^T R - 2SD_d$ is a positive definite matrix. If this condition is fulfilled, the equilibrium point is globally asymptotically stable based on LaSalle's invariance principle. Because the equilibrium points cannot be derived analytically and the system is hybridized, we conducted simulations to evaluate the proposed controller.

4.4 Simulation Setup

4.4.1 Dimensionless Model

The parameters m, l, and $\sqrt{l/g}$, characteristic mass, length, and time scale of the model, respectively, are converted to dimensionless parameters as $m_i^* = m_i/m$, $I_i^* = I_i/(ml^2)$, $k^* = k/(lmg)$, $d^* = d/(lm\sqrt{lg})$, $k_g^* = lk_g/(mg)$, and $d_g^* = d_g\sqrt{lg}/m$ to decrease the number of parameters that must be investigated. The other variables were represented as $F^* = F/(mg)$, $\dot{()}^* = \sqrt{l/g}\,\dot{()}$, $\theta^* = \theta$, and $t^* = t\sqrt{g/L}$. Subsequently, the dimensionless equation of Eq. 6 was derived by dividing Eq. 6 by lmg.

4.4.2 Physical Parameters

The length of link l was determined by balancing the approximation accuracy and computational cost to discretize the continuum body. The accuracy of the representation of the continuous curve improves and the degree of freedom of the movement increases if the length of the links decreases; however, the cost of the numerical calculation increases. In this study, we selected $l = 50$ mm because the discrete model can approximate a half circle with a length of 1 m with an error < 1 mm (0.1% of the entire length), which is sufficiently accurate for our requirements. Additionally, we confirmed that the tendencies of the equilibrium points and stability did not change when l decreased as explained in Appendix B.

The physical parameters of the model were determined based on the developed robot, as listed in Table 1. The total length of the model was set to 1 m ($N = 20$). Based on the

Table 1 Physical parameters used for simulations

Element	Value	Element	Value
l [m]	0.05	k^*	94.4
m [kg]	0.0166	I_i^*	$m_i^*(1 + 3\phi_r^{*2}/4)/12$
g [m/s^2]	9.8	k_g^*	3×10^3
N	20	d_g^*	$2\sqrt{k_g^*}$
m_1^*	3.62	d^*	parameter

robot, we set the mass of the link to $m = m_i = 16.6\,\text{g}\ (i \neq 2)$ and the gravitational acceleration to $g = 9.8$ m/s^2. The head of the robot was slightly heavier than its body because it was equipped with a camera and other sensors. Thus, we set $m_1 = 60$ g, based on the robot. The moment of inertia was set to $I_i^* = m_i^*(1 + 3\phi_r^{*2}/4)/12$, and calculated as a uniform cylinder with a diameter of $\phi_r = 40$ mm. The spring stiffness and damper coefficient of the ground (k_g^* and d_g^*) were set to large values equal to $\sim 10^3$. The spring stiffness k^* was estimated as $k^* = 94.4$ by measuring the static property of the ASC tube (200 mm).

In this simulation, we changed d^* to a parameter because the damper coefficient is important for determining the stability of the equilibrium points.

4.4.3 Stability Analysis Method

We applied linear stability analysis based on a Jacobian matrix to evaluate the stability of the system. The Jacobian matrix was defined according to the equation of motion in Eq. 6.

Let $z = [\boldsymbol{\theta}^T\ \dot{\boldsymbol{\theta}}^T]^T \in \mathbb{R}^{2N \times 1}$ be the state vector of the system. Equation 6 can then be rewritten as $\dot{z} = h(z)$, where $h \in \mathbb{R}^{2N \times 1}$ denotes a nonlinear vector function. If the equilibrium point is derived as z^* ($0 = h(z^*)$), then Jacobian matrix J_c is defined as $J_c = \frac{\partial h}{\partial z}|_{z=z^*}$. The eigenvalues of the Jacobian matrix specify the linear stability of a system [46]. If the maximum of the real parts of all eigenvalues is less than zero, then the equilibrium points of the system are linearly stable. Further, the real parts of the eigenvalues are related to damping.

4.5 Simulation Results

We evaluated the equilibrium points and their stability using the proposed controller. The physical parameters were the same as those listed in Table 1. The input force was controlled as $(F_x^*,\ F_y^*) = (F^* \sin \psi,\ F^* \cos \psi)$, and the direction of the force ψ was set to $\psi = \pi/9$, similar to that for the robot. We searched for equilibrium points and evaluated the linear and global stabilities for F^* with various d^* values.

Fig. 3 (A) Head heights and (B) shapes of model for equilibrium points. The height of the head tip increased as the force increased
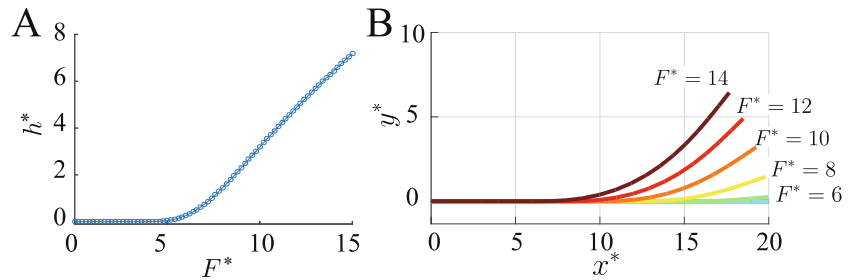
We found stable equilibrium points for various head tip heights h^* at various F^* values. Figure 3A shows the h^* values of the identified equilibrium points. The shapes of the model for various equilibrium points are shown in Fig. 3B. Figure 4A shows the maximum real parts of the eigenvalues of the Jacobian matrix when $d^* = \{100, 200, 300, 400\}$. All equilibrium points are linearly stable because the eigenvalues are less than 0. The eigenvalue exhibits abrupt changes at some points because of the changes in the number of links on the ground. Figure 4B shows the minimum eigenvalues of $kR^T R - 2SD_d$ Eq. 14. The number of floating links N_{air} used to calculate Eq. 14 was estimated using the simulation results. For $F^* < 14$, the signs of the eigenvalues are positive and fulfill the sufficient condition for global stability.

These figures indicate that the controller can elevate the head by more than 300 mm ($h^* = 6$) in a stable manner. The head levitated higher as the force increased. Global stability is also ensured for $F^* < 14$ while all identified solutions are locally stable. Further, Fig. 4A indicates that when the force is small, a smaller damper coefficient produces larger stability, whereas a larger damper produces larger stability for a large force. We believe that an increase in the number of floating links changes the dominant mode of the oscillation which affects stability. However, in practice, a larger damper coefficient is feasible for the robot because it offers better stability when the front tip is in the air.

Finally, various parameters were evaluated using the same simulation to assess the effectiveness of the controller subject to parametric variations. As d^*, m_1^*, ψ, and F^* change depending on the robot design, we changed these parameters, as listed in Table 2. We simulated all the combinations

of these parameters ($4 \times 19 \times 19 \times 76$) and found that the equilibrium points existed in all cases and were locally stable.

The simulation depends on a simple model that is slightly different from an actual robot system, which is a limitation. The robot moved in a three-dimensional space, and the ground surface was a complicated terrain. Furthermore, the robot was longer (7 m) than the model and moved forward. We did not investigate the stability when the model's root was moved. However, the simple model extracted the essential points to realize stable levitation and derived a simple directional controller. We also evaluated the practicality of the controller in a step-climbing experiment in Section 6.

5 Stabilized Levitation with a Passive Mechanism

5.1 Proposed Passive Mechanism

We propose a passive mechanism to realize a lightweight controller. The mechanism comprises a passive joint and wires, as shown in Fig. 5. The head with the nozzle was connected to the body with a passive joint to enable a large rotation. The wires were threaded through guides on the body surface, and their ends were fixed to the head and body. The lengths of the wires were the same as the length of the center curve of the body between the fixed-wire points.

This mechanism constrained the head posture to be parallel to the wire-fixed point on the body, which was (in turn) constrained to the direction of the air jet. Theoretically, if the center curve is differentiable and the wires are threaded

Fig. 4 Variation of stability as a function of force F^* for various d^* values. (A) Maximum real parts of the eigenvalues of the Jacobian matrix for F^*, when $d^* = \{100, 200, 300, 400\}$. (B) Minimum eigenvalues of $kR^T R - 2SD_d$ Eq. 14 used to evaluate global stability
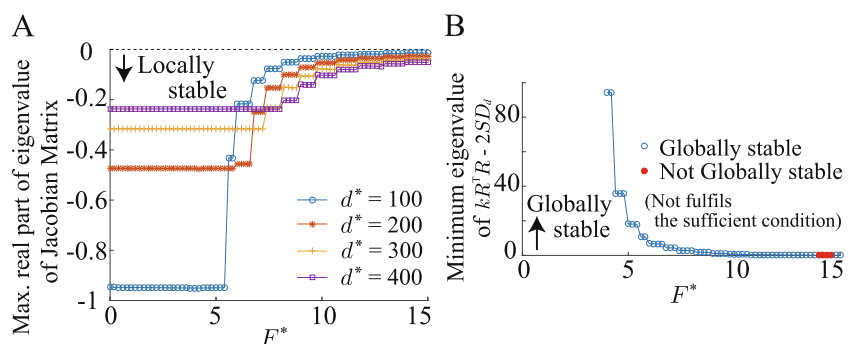
Table 2 Simulation parameter sets

Parameter	Value	Number
d^*	{100, 200, 300, 400}	4
m_1^*	{1, 1.5, $\cdots$, 10}	19
ψ	{0, $\pi/36$, $\cdots$, $\pi/2$}	19
F^*	{0, 0.2, $\cdots$, 15}	76

along the body surface continuously, the wires can constrain the head posture to be completely parallel to the wire's fixed point.

The robot, which operates based on this mechanism, is shown in Fig. 1C. The parameters were the same as those described in Section 4.4. Wires were threaded through the guides on the tube at 50 mm intervals, and both ends of the wires were fixed to the head and body (1 m from the head).

5.2 Experimental Evaluation of Mechanism and Head Levitation

5.2.1 Experimental Setup

We conducted experiments using the robot to validate the stabilized levitation and passive mechanism. For the experimental setup, we fixed the robot at a position 1 m behind the head on horizontal ground and investigated the shape of the equilibrium points (to determine whether the robot floated stably) by applying various air pressures. Posture sensors were installed on the head and the front parts of the body, as shown in Fig. 5. In each trial, the head was laid on horizontal ground. Subsequently, we gradually increased the air pressure to a particular value. Finally, the head and front body postures and the height of the head were measured when the robot floated statically. In addition, we mapped the air pressure and magnitude of the jet force in advance.
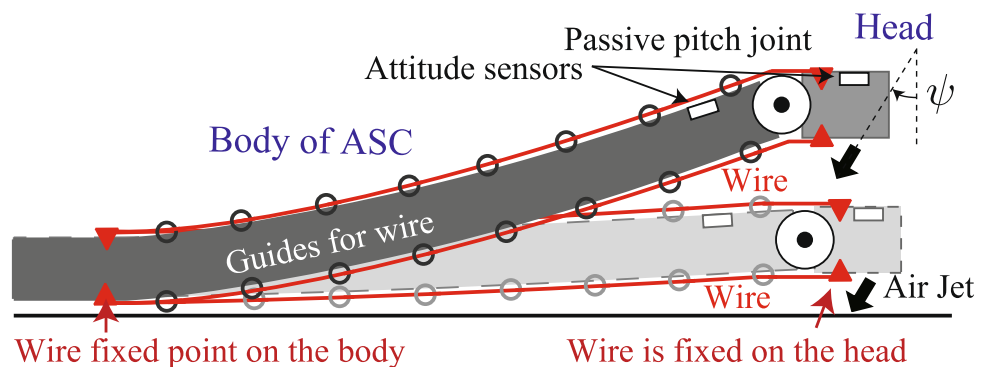
5.2.2 Evaluation of Passive Mechanism

First, we confirmed that the proposed passive mechanism was effective. The relationship between the measured pitch angles and head height h^* at the equilibrium points is shown in Fig. 6A. The blue circles indicate the pitch angles of the head and the red asterisks represent those of the anterior part of the body. When the head was elevated from $h^* = 0$ to $h^* \sim 4$, the pitch angle of the front part changed substantially (approximately $\pi/6$ rad), whereas the pitch angle of the head changed slightly (approximately $\pi/18$ rad). Although the head posture was not constrained to be parallel to the ground, the proposed passive mechanism was effective. For the preparation of the simulation in the next section, we determined the relationship between the direction of the air jet ψ and the magnitude of the applied force F^*, as shown in Fig. 6B.

This discrepancy in head posture was due to hardware limitations. The wire could not follow the surface continuously because of discrete wire guides. The passive pitch joint makes the center curve undifferentiable. However, the posture of the head is well-constrained by the mechanism, and it can passively stabilize the levitated head.

5.2.3 Evaluation of Equilibrium Points

We plotted the relationship between the input forces F^* and head height of the equilibrium points h^* in the experiments and the simulations. The measured height h^* in relation to F^* is indicated by the blue circles in Fig. 7A (also plotted in Fig. 7B). In Fig. 7A, the simulation results for various masses m_1^* are shown, and the other parameters are listed in Table 1. In Fig. 7B, the simulation results for various force directions ψ with $m_1^* = 6$ are shown. The green line in Fig. 7B shows the result in the case in which $\psi(F)$ was estimated using the fitted line in Fig. 6B.

Equilibrium points existed for all reaction forces, and a larger force elevated the head higher. The tendency of the simulation results with the parameters listed in Table 1(solid red line in Fig. 7A) was different from that of the experiment

Fig. 5 Overview of the mechanism. A wire was connected between the body and front part. The wire is threaded through the guides (black circles). This mechanism constrains the pose of the head to be almost parallel to the wire-contact point of the body

Fig. 6 (A) Relationship between measured pitch angle and tip height h^* at equilibrium points. The blue circles represent the pitch angles of the head. The red asterisks represent those of the front part of the flexible body. (B) Relationship between the air-jet direction ψ and force F^* at equilibrium points. The circles represent the measured data for ψ. The line represents a linear regression
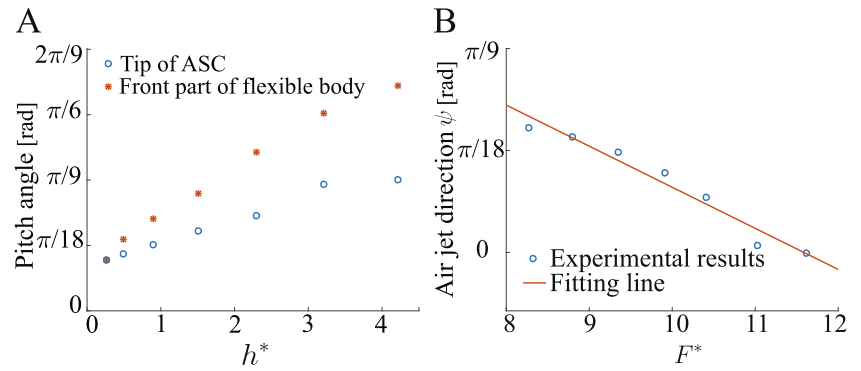
from two aspects: (1) the value of F^* when the head lifted off was different, and (2) the gradient of the graph was different. However, (1) F^* at the head liftoff approaches the experimental value when the head gets heavier, as shown in Fig. 7A, and (2) the gradient of the graph becomes closer to the experimental when using the estimated $\psi(F)$, as shown in Fig. 7B.

The discrepancies in the equilibrium points result from the underestimation of the head weight and air-jet directional errors. We modeled the body as a series of uniform links; however, for the actual test bed, the front part was heavier than the other parts owing to the installed vibration motor and circuits. This model limitation needs to be addressed in the future.

5.3 Experimental Evaluation of Stability

5.3.1 Experimental Setup

The body was fixed on a horizontal plane 1 m from the head. First, we constrained the initial posture of the ASC using a bar and set the magnitude of the force to a certain value ($F^* = 10.4$). We then removed the bar and measured the temporal response of the posture sensor installed on the front part of the body. Furthermore, we conducted a simulation with the parameters $m_1^* = 6$ (from the previous section), $\psi = 0.0951$ (fitted-line value when $F^* = 10.4$ in Fig. 6B),

and $d^* = 300$. The other parameters were the same as those listed in Table 1. The initial state variables of the simulation were approximated as the nearest equilibrium points based on experiments.

5.3.2 Evaluation of stability

Figure 8A shows the temporal response of the measured pitch angle, and Fig. 8B shows the response of the pitch angle of the head link θ_1 in the simulation. In Fig. 8A, the pitch angle converges over time for all initial values. Only 3.16 s ($t^* = 44.2$) were required until the given disturbances decreased to values less than 10 % of the initial disturbances. However, different initial values caused the converged points to differ. In the simulation, the pitch angle converged to a particular value, regardless of the initial values in Fig. 8B.

This settling time (3.2 s) is sufficiently small for practical use because the ratio of the settling time to typical inspection time was less than 0.5% (the inspection time was in the range of 14–30 min regarding the trials in the inspection cases of collapsed houses caused by the Kumamoto Earthquake 2016 [20]).

The discrepancy in the response to the disturbance was attributed to the existence of friction. The friction between the wires and guides changed the converged points depending on the initial values, thus making precise height control challenging. However, if we approximate friction as a damping

Fig. 7 Height of the ASC head h^* as a function of the force F^* at equilibrium points in experiments and simulations. The circles represent the experimental data. The lines represent the results from simulations using various parameters. (A) The simulation results shifted to the right as the mass m_1^* increased. (B) The gradient of the simulation results increased as the force direction ψ decreased
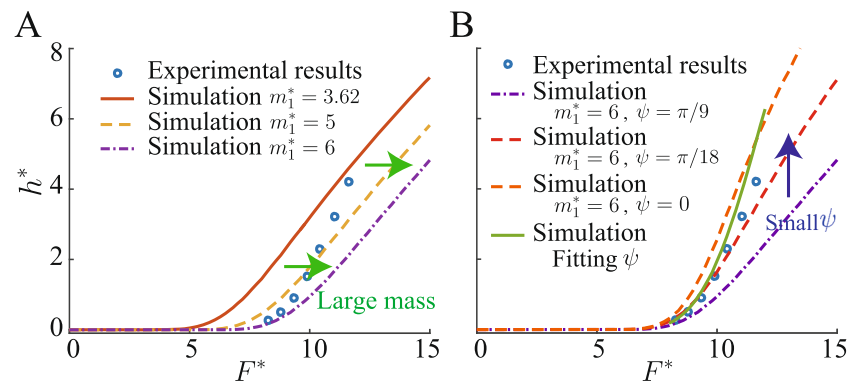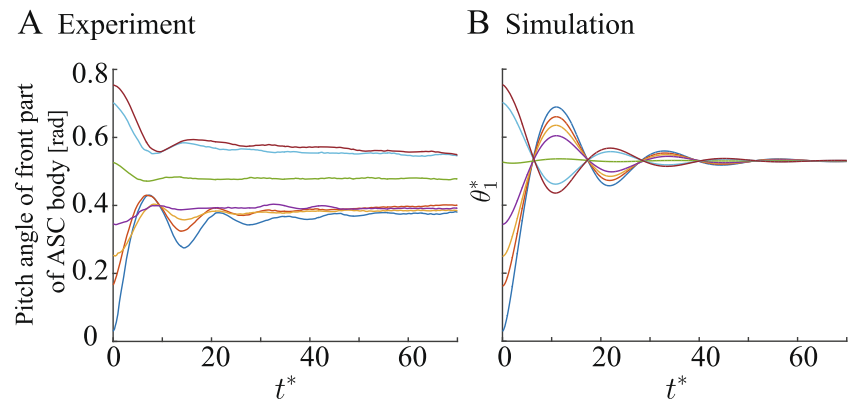
Fig. 8 Time response of pitch angle. (A) Pitch angle measured using a posture sensor placed on the front part of the body. (B) Simulated pitch angle θ_1^* outcomes

term, as indicated by some studies [45, 47], it contributes to stability improvements at some ranges, as shown in Fig. 4. Our system prioritizes damping of the head vibration over precise head height control. If there is a head height error, the operator can easily adjust the height by adjusting the air pressure. However, if severe head vibration occurs, the operator must stop the exploration until the vibration stops to minimize the risk of backward bending motion, collision, and lousy situation awareness due to the vibrating camera image. Therefore, we believe that friction is beneficial for our system.

5.4 Discussion on Stabilized Levitation

We confirmed that the nozzle elevated the head by more than 200 mm as the pressure increased, and the mechanism stabilized the levitated head. Although the equilibrium points and temporal response to a disturbance in the experiments were slightly different from those in the simulations, the causes could be explained.

One limitation pertains to the fact that a constant air-jet direction cannot be achieved if the postures (pitch and roll) of the wire-fixed point change as the robot moves, which may prevent stable head levitation. However, the mechanical structure is simple, lightweight, and can be easily installed on the robot. Furthermore, this limitation can be overcome if we operate the robot to avoid these scenarios (i.e., moving slowly while maintaining the roll posture by twisting the robot and adjusting the air pressure depending on the pitch posture), as discussed in Section 6.

6 Step Climbing Experiments

6.1 Robotic System

The robotic system for the experiment is shown in Fig. 9A. The developed ait-floating-type ASC passed through a

robotic thruster [48], which could thrust and twist the body of the ASC from the posterior part. The moving functions for the robotic system included five elements: (1) propelling motion of the body by adding body vibration (cilia-driving mechanism [19]), (2) head height changes achieved by adjusting air pressure, (3) head steering achieved by adjusting the nozzle's rotational angle along the longitudinal axis (Fig. 1C), (4) pushing motion of the body achieved by using the robotic thruster, and (5) twist motion of the robot's body achieved by using the robotic thruster [48].

In the experiment, we automated robotic control for as long as possible to evaluate the mobility of the robot quantitatively. The block diagram of the control system is shown in Fig. 9B. The operator controlled only two elements: the air pressure to control the head height and nozzle's rotational angle to steer the robot to move forward. The ranges of these inputs were [0.0, 0.6] MPa and [-0.7, 0.7] rad. The strength of the vibration was maintained at the maximum value (approximately 60 Hz), and the thrust speed was kept constant at 40 mm/s; this speed was lower than the body's moving speed achieved by the cilia-driving mechanism. The twist angle was controlled by a proportional derivative controller (PD controller) to maintain the head-roll posture at 0 rad. This is because we modeled and designed the mechanism in the sagittal plane, which ignored the rotation of the robot's body along the longitudinal axis. The head posture was measured by the inertia measurement unit (MPU-9250) on the head, and the twisting velocity input (rad/s) of the thruster was calculated by the PD controller with the gains of 1.7 (P gain) and 0.57 (D gain) at the control frequency of 100 Hz.

6.2 Experimental Setup

A planar step (0.8 m × 1 m) was set on the horizontal ground at various heights, as shown in Fig. 10A. The route of the robot on the ground was guided by 1 m long wooden sticks with a height of 20 mm; these sticks were placed parallel from each other at a distance of approximately 100 mm and 0.5 m away from the step. These sticks emulate the constraints

Fig. 9 Experimental system for the step climbing. (A) Robot system which has five moving functions, and (B) block diagram of the control system in the experiment

A   Five moving functions of robot system
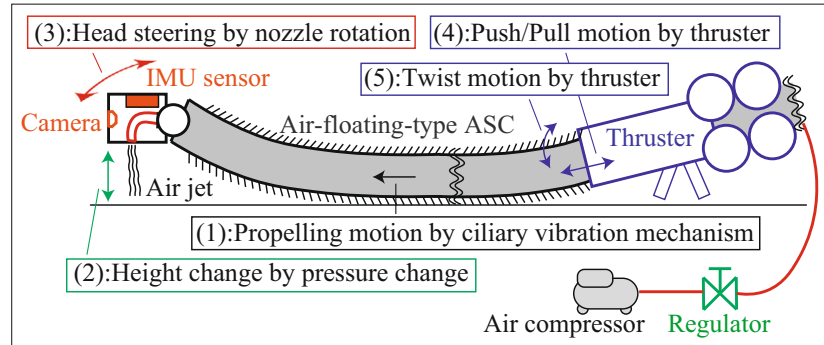
B   Block diagram of the experimental system
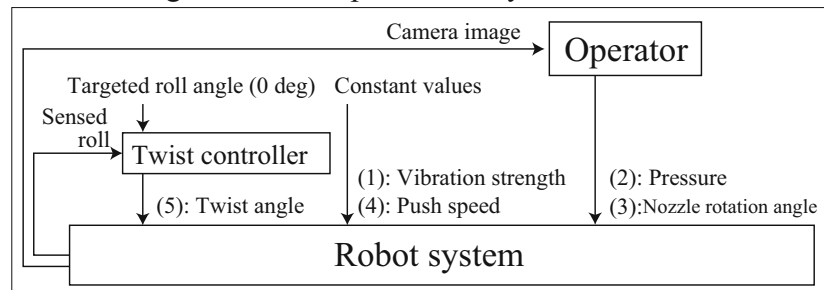
caused by the rubble on the ASC body. The ASC was pushed to the step by the robotic thruster. We placed the outlet of the robotic thruster on the ground and at a distance of 1.5 m away from the step. We define the coordinates $O-xyz$ as shown in Fig. 10A.

In each trial, the robot started at a point 0.5 m away from the step. The operator then controlled the nozzle's rotational angle and air pressure by viewing the image from the video scope. We assumed that the robot moved over the step when the head reached the end (moved forward by 1 m on the step). We measured all the inputs and robotic positions using sensors. Specifically, pressure was measured using *ITV3050* (*SMC Corporation*), nozzle rotation angle was estimated by counting the pulses of the encoder, and head position, head posture, and posture of the wire-fixed point on the body were determined using a motion capture system (*Vantage V5, Vicon Motion Systems Ltd.*). This process was repeated five times for each step height. We varied the step height for four patterns: 150, 200, 250, and 300 mm.

As a typical example, we present the temporal responses of the measured values for the trial with a step height of 200 mm (Supplementary video is available). Snapshots of climbing are shown in Fig. 10A, and the trajectory of the head is shown in Fig. 10B. The red and green points represent the locations where the head reached the step edges. The temporal responses of the inputs (air pressure and nozzle rotation angle) and positions of the head (z and y) are shown in Fig. 10C and D. The temporal responses of the measured postures (roll and pitch angles) at the head and wire-fixed points are shown in Fig. 10E.

For approximately 0–7 s, the operator increased the air pressure gradually up to 0.45 MPa (Fig. 10C1), and the air jet lifted the head in a stable manner (without severe vibration) to a height > 200 mm, as shown in Fig. 10D1. For approximately 7–10 s, the head moved forward at an almost constant speed owing to the thrust from the root (Fig. 10D1). At approximately 9 s (red dashed lines), the head reached the step. For approximately 10–15 s, the body leaned toward

6.3 Results

Table 3 lists the success ratio for moving over the step depending on its height. The robot could move over steps with heights up to 200 mm without failure. Further, we confirmed that the previous ASC, whose head could be bent by a pneumatic actuator [18], could not move over steps (even those with heights equal to 50 mm) in other experiments.

Table 3 Robot success ratios for moving over steps

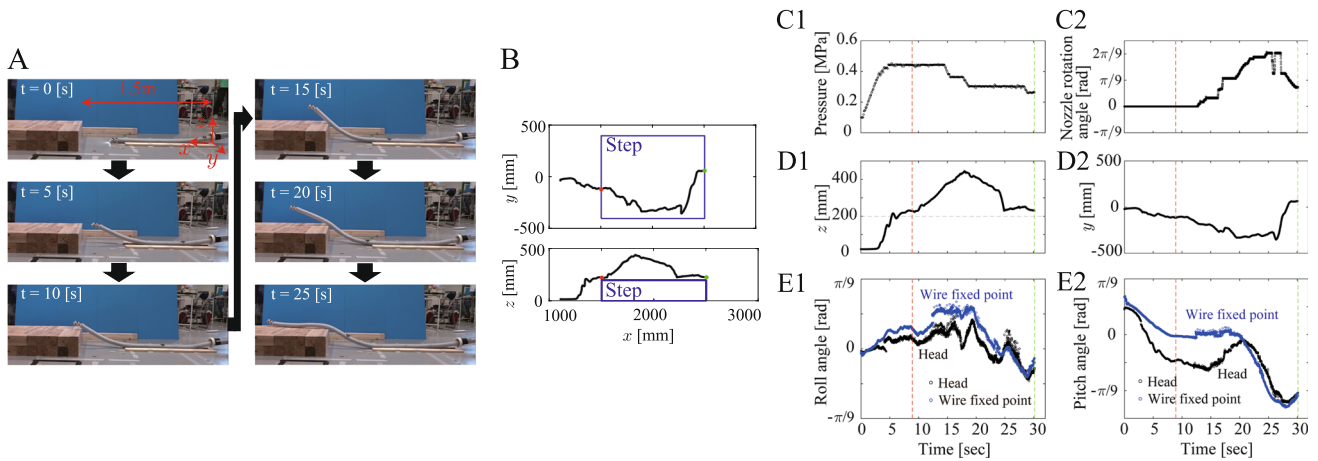| Step height [mm]	Success ratio
150	5/5
200	5/5
250	4/5
300	0/5

Fig. 10 Experimental results obtained during the climbing of a step with a height equal to 200 mm. (A) Snapshots of movement, (B) trajectory of the robotic head, (C) temporal responses of operator's inputs (C1: air pressure and C2: nozzle's rotational angle), (D) temporal responses of head positions (D1: height (z) and D2: lateral length (y)), and (E) temporal responses of the head posture (black points) and posture of wire-fixed point (blue points) (E1: roll and E2: pitch angles)

the edge of the step (Fig. 10A). The head height increased, and the pitch angle decreased (Fig. 10D1 and E2) while the pressure was constant (Fig. 10C1). In addition, the head's y position started decreasing (Fig. 10D2) because of the body's interaction with the step edge. For approximately 15–20 s, the operator found that the head height increased (determined based on camera image measurements), the operator decreased the pressure (Fig. 10C1), and the head pitch angle increased (Fig. 10E2). In addition, the operator commanded the nozzle rotation (Fig. 10C2 and D2) to adjust the moving direction of the head. Without steering, the head easily slid down along the y direction because of its interaction with the step edge. For approximately 20–30 s, the wire's fixed point began to lean toward the step, and the pitch angle of the wire's fixed point decreased for approximately $\pi/9$ (Fig. 10E2); this could cause the backward bending motion if the jet direction had faced forward owing to the passive mechanism. However, the robot could avoid backward bending because the operator decreased the air pressure in advance. At 30 s, the wire's fixed point moved on the step, which means that the robot successfully moved over the step. Furthermore, we note that the thruster maintained a head-roll posture in the range of $\pm\pi/18$ rad, as shown in Fig. 10E1.

We show the snapshots of the robot climbing on a step with a height of 300 mm in Fig. 11 as an example of a typical, failed climbing attempt. For approximately 0–10 s, the robot elevated the head to 300 mm and stepped the head on the step (10 s). Then, at approximately 15–20 s, the robot body bent at a more significant curvature between the step edge and the ground, and the head was directed almost vertically as the body moved forward. Although the operator attempted to control the air-jet direction to maintain this posture against gravity, the head finally fell (25 s) and failed the climbing.

6.4 Discussion

We confirmed that stable head floating enabled the robot to move over steps with heights up to 250 mm, which was impossible to achieve with the previous ASC. Furthermore, the limitations discussed in the previous sections could be compensated when specific operation techniques were used. For example, the limitation of the passive mechanism can be overcome by adjusting the air pressure based on the head posture (Fig. 10E2). In another example, the maximum torsional angle of the levitated part (angle between the head and the wire-fixed point)(ignored in the model) was less than approximately $\pi/18$ rad, as shown in Fig. 10E1. This value is practically small because the passive mechanism works effectively (the pitch angles of the head and wire-fixed points are almost the same (the approximate difference is $\pi/18$ rad,
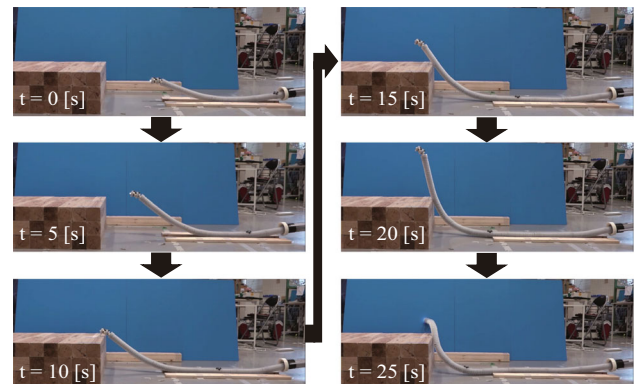

Fig. 11 Snapshots of failed climbing movements on a step with a height of 300 mm

as shown in Fig. 10E2)), and stabilized head floating was achieved during the experiment.

The step climb failures are characterized by the large curvature of the body's shape between the step edge and the ground. This curvature results in the rotation of the tip of the body in the vertically upward direction, which increases the risk of falling. The likelihood of the occurrence of this phenomenon increases as the step height increases. To avoid the failure to climb higher steps, an additional air-jet nozzle can be attached to the middle part of the body to levitate the body to reduce the aforementioned bending curvature. Another effective solution is to install a variable stiffness mechanism on the body (such as [49, 50]). The stiffened body can suppress undesirable bending during step climbing.

7 Demonstration on Rubble

To assess the mobility responses in a realistic environment, this section discusses two mobility demonstrations in wooden and concrete rubble. In both cases, the robot was inserted through a pipe by a person (inserter), and the air pressure and nozzle direction were controlled by another person (operator).

We tested the mobility in the wooden rubble environment, which was developed by imitating the collapsed wooden buildings by earthquakes as Fig. 12 [20]. The field consisted of wooden blocks with a maximum height of approximately 300 mm. The robot moved approximately 2 m. It took approximately 45 s to cover the field. Snapshots of the movement are shown in Fig. 12 (Supplementary video). Using its stabilized head floating and direction control, the robot could climb the rubble after choosing an appropriate path.

In the case of the concrete rubble, the robot moved approximately 4 m, as shown in Fig. 13. The field consisted of concrete blocks with gaps between them (approximately equal to 200 mm). It took approximately 50 s to cover the field. Snapshots of the movement are shown in Fig. 13 (Supplementary video). Using the head floating and direction control, the robot could move between the gaps.

We confirmed that the robot head can float stably even on these irregular terrains, and the robot can move over some steps and gaps, thus improving considerably its ability to access the rubble. One of the important lessons learned from the demonstration in rubble is that trajectory planning is key for the robot's mobility. For example, if the robot chooses a trajectory such that the contact area between the body and rubble is small, the robot will be unable to move over some steps because of the low cilia-driving force on the body. In view of these, we would like to discuss and formulate a strategy for the robot for future applications.
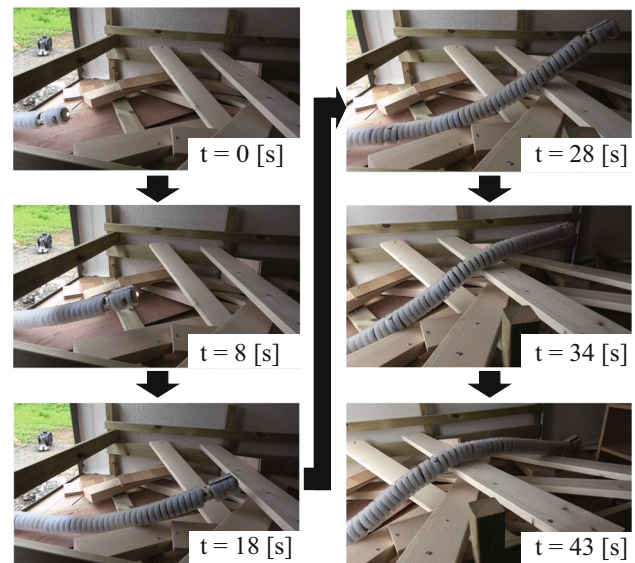

Fig. 12 Snapshots showing wooden rubble. The stabilized head floating and direction control allow the robot to climb steps with a maximum height approximately equal to 300 mm

8 Conclusions and Future Work

We developed an air-jet-actuated continuum robot that can elevate its head and climb steps, thereby improving mobility in the rubble. First, we proposed a simple directional controller that maintained a constant thrust direction relative to gravity (not the magnitude of thrust) on a sagittal plane; the sufficient condition for global stability was derived analytically. The stability of head levitation was validated
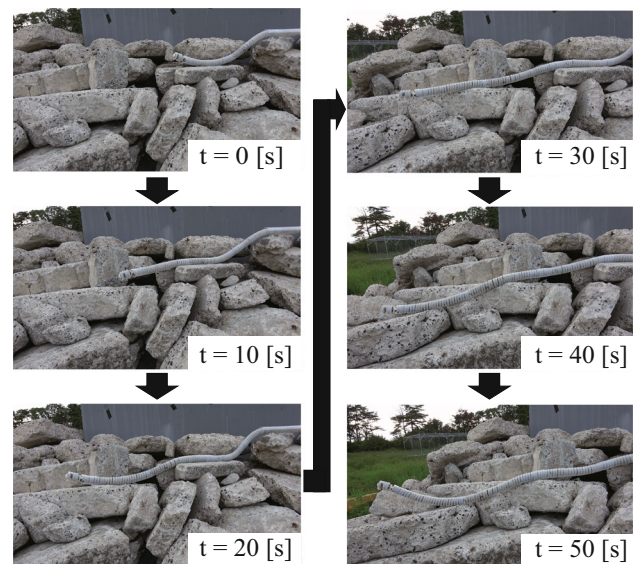

Fig. 13 Snapshots showing concrete rubble. The head floating and direction control allow the robot to move over gaps with lengths which are approximately equal to 200 mm

based on simulations. Second, thanks to the simplicity of the controller, the developed robot used a lightweight passive mechanism without motors. This mechanism maintains the head posture (direction of the nozzle outlet) parallel to the ground by using wires. We demonstrated that the mechanism could stabilize the levitating head with the developed air-floating-type ASC. Third, quantitative experiments showed that the robot could climb steps with heights up to 250 mm. Improved performance is thus demonstrated compared with that of the previous ASC. Some demonstrations on rubble validated the high mobility of the robot. This jet's directional controller is expected to contribute to future enhancements of the mobility of continuum robots owing to its simplicity and practicality. In the future, we need to propose a more specific control strategy for step climbing with head levitation, as well as the three-dimensional movement of the head.

Appendix A

In this Appendix, we derive the sufficient condition for the function E' Eq. 11 to be positive definite. The first term of Eq. 11, T, fulfills the condition $T \geq 0$ in Eq. 1, and equality is attained if and only if $\dot{\boldsymbol{\theta}} = 0$. Thus, we need to derive the sufficient condition for the second term $V'(\boldsymbol{\theta}) - V'(\hat{\boldsymbol{\theta}}) \equiv V''$ to be positive definite.

The potential function V'' can be expanded as

$$V''(\Delta\boldsymbol{\theta}) = \frac{1}{2}k(\Delta\boldsymbol{\theta})^T R^T R(\Delta\boldsymbol{\theta})$$
$$+\sum_i d_i \left\{ (\sin \Delta\theta_i - \Delta\theta_i) \sin \hat{p}_i + (1-\cos \Delta\theta_i) \cos \hat{p}_i \right\},$$

where $\Delta\theta_i = \theta_i - \hat{\theta}_i$, $\hat{p}_i = \hat{\theta}_i + \psi_i$, and d_i and ψ_i are as defined in Section 4.2. The above equation can be expanded by defining a constant variable $s_i \geq 0$ as

$$V'' = \frac{1}{2}(\Delta\boldsymbol{\theta})^T (kR^T R - 2SD_d)(\Delta\boldsymbol{\theta}) + \sum_i d_i f_i(\Delta\theta_i)$$

$$f_i(x) = s_i x^2 + (\sin x - x)\sin \hat{p}_i + (1 - \cos x)\cos \hat{p}_i \quad \text{(A1)}$$

where $S = \text{diag}(s_i)$ and $D_d = \text{diag}(d_i)$. Herein, we derive the sufficient condition for the function V'' to be positive definite because it is considerably difficult to derive a necessary and sufficient condition as $V''(x)$ contains $\sin x, \cos x, x$ (transcendental equation).

First, we derived the sufficient condition of s_i, in such that the second term $\sum d_i f_i(\Delta\theta_i)$ was not negative, as indicated in Lemma 1. We then derived the necessary and sufficient condition for the first term to be positive definite with the specific s_i that fulfilled the Lemma. Therefore, the sufficient

condition for the positive definiteness of V'' was derived according to Theorem 2.

Lemma 1 *(Sufficient condition for $f_i \geq 0$) For the function $f_i : \mathbb{R} \rightarrow \mathbb{R}$, defined as Eq. A1, the sufficient condition for $f_i(x) \geq 0$ for an arbitrary $x \in \mathbb{R}$ is*

$$s_i \geq \begin{cases} \frac{1}{2}|\sin \hat{p}_i|, & \cos \hat{p}_i \geq 0 \\ \frac{1}{2}, & \cos \hat{p}_i < 0 \end{cases} \quad \text{(A2)}$$

Proof f_i satisfies the following inequality.

$$f_i(x) = s_i x^2 + (\sin x - x)\sin \hat{p}_i + (1-\cos x)\cos \hat{p}_i$$
$$\geq s_i|x|^2 + (\sin|x| - |x|)|\sin \hat{p}_i| + (1-\cos|x|)\cos \hat{p}_i,$$
$$\text{(A3)}$$

which is derived using $\sin|x| - |x| \leq \sin x - x \leq -\sin|x| + |x|$

We thus prove that Eq. A2 is a sufficient condition by case analysis.

Case 1: $\cos \hat{p}_i \geq 0$

Because the third term of Eq. A3 is non-negative, we only analyzed the function $g_i(x)$ and showed $g_i(x) \geq 0$ for $x \geq 0$ in the sufficient condition.

$$g_i(x) = s_i x^2 + |\sin \hat{p}_i|(\sin x - x) \quad \text{(A4)}$$

The first and second derivatives of the function $g_i(x)$ can be derived as

$$\dot{g}_i(x) = 2s_i x + |\sin \hat{p}_i|(\cos x - 1), \quad \text{(A5)}$$
$$\ddot{g}_i(x) = 2s_i - |\sin \hat{p}_i|\sin x. \quad \text{(A6)}$$

When the sufficient condition is fulfilled ($s_i \geq |\sin \hat{p}_i|/2$), $\dot{g}_i(x)$ satisfies $\dot{g}_i(x) \geq 0$ because $\ddot{g}_i \geq 0$ and $\dot{g}_i(0) = 0$. In addition, $g_i(x)$ satisfies $g_i(x) \geq 0$ because $\dot{g}_i(x) \geq 0$ and $g_i(0) = 0$. This implies that $f_i(x) \geq 0$ if $s_i \geq |\sin \hat{p}_i|/2$.

Case 2: $\cos \hat{p}_i < 0$

Because the third term of Eq. A3 is not positive, we analyze the function $h_i(x)$ and show $h_i(x) \geq 0$ for $x \geq 0$ in the sufficient condition case.

$$h_i(x) = s_i x^2 + |\sin \hat{p}_i|(\sin x - x) + |\cos \hat{p}_i|(\cos x - 1). \quad \text{(A7)}$$

The first and second derivatives of the function $h_i(x)$ can be derived as

$$\dot{h}_i(x) = 2s_i x + |\sin \hat{p}_i|(\cos x - 1) - |\cos \hat{p}_i|\sin x, \quad \text{(A8)}$$
$$\ddot{h}_i(x) = 2s_i - (|\sin \hat{p}_i|\sin x + |\cos \hat{p}_i|\cos x) \quad \text{(A9)}$$

When the sufficient condition is fulfilled ($s_i \geq 1/2$), $\ddot{h}_i(x)$ fulfills $\ddot{h}_i(x) \geq 0$ because the second term of Eq. A9

$((|\sin \hat{p}_i| \sin x + |\cos \hat{p}_i| \cos x))$ is not greater than one. Therefore, the relationship $\dot{h}_i(0) = 0$ yields $\dot{h}_i(x) \geq 0$.

In addition, $h_i(x)$ satisfies $h_i(x) \geq 0$, because $\dot{h}_i(x) \geq 0$ and $h_i(0) = 0$. This implies that $f_i(x) \geq 0$ if $s_i \geq 1/2$. □

The following theorem can be proved using the Lemma.

Theorem 2 *(Sufficient condition for positive definiteness of V'') For the function $V'' : \mathbb{R}^N \to \mathbb{R}$, defined as Eq. A1, the sufficient condition for $V''(x)$ to be a positive definite function is inequality Eq. A10.*

$$kR^T R - 2SD_d > 0, \tag{A10}$$

where $S = \text{diag}(s_i)$ and

$$s_i = \begin{cases} \dfrac{1}{2}|\sin \hat{p}_i|, & \cos \hat{p}_i \geq 0 \\ \dfrac{1}{2}, & \cos \hat{p}_i < 0 \end{cases}. \tag{A11}$$

The sign of the inequality in Eq. A10 implies that matrix $kR^T R - 2SD_d$ is a positive definite matrix.

Proof If the sufficient condition $(kR^T R - 2SD_d > 0)$ is fulfilled, the first term of V'' (Eq. A1) is a positive definite function. The second term of V'' (Eq. A1) is proved not to be negative for s_i in Eq. A11 using Lemma 1 and the relation $d_i > 0$. Thus, $V''(x) \geq 0$, and the equation is attained only when $x = 0$, which implies that V'' is a positive definite function. □

Appendix B

Figure 14 shows how the equilibrium points, linear stability (maximum real part of the eigenvalue of the Jacobian matrix), and global stability (minimum eigenvalue of $kR^T R - 2SD_d$) against F^* change as the number of links changes. The simulation setup is the same as that used in Figs. 3 and 4 ($d^* = 200$) except that the head link weight is set as the same weight as the body links for the comparison. The tendency of the equilibrium height against F^* when $N = 20(l = 50$ mm) corresponds well with that of $N = 50(l = 20$ mm). The maximum difference of the equilibrium height is less than 0.05% of the entire length. For linear and global stability, the result with $N = 20$ has a similar tendency to that of $N = 50$ when F^* is larger than three, although there is a discrete gap when the number of floating links changes. However, the difference is rather large, especially when the F^* value is less than three, because the number of floating links is small. The authors think this difference is affordable because we are mainly interested in the case where the head
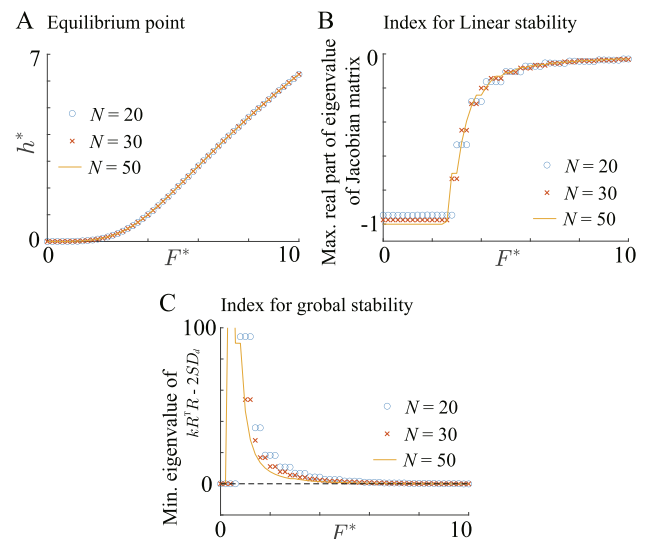

Fig. 14 Head height (A), linear stability (B), and global stability (C) of equilibrium point against the magnitude of input force depending on the number of links

height is adequately high to allow the robot to climb over the step (h^* is approximately equal to four).

Declarations

Ethics approval Not applicable.

Consent to participate Not applicable.

Consent to publish Not applicable.

Competing interests The authors have no relevant financial interests to disclose.

References

1. Ackerman, E.: What CMU's snake robot team learned while searching for Mexican earthquake survivors. IEEE Spectr. Newsl. (2017)

2. Tadokoro, S., Murphy, R., Stover, S., Brack, W., Konyo, M., Nishimura, T., et al.: Application of active scope camera to forensic investigation of construction accident. In: 2009 IEEE Workshop on Advanced Robotics and its Social Impacts, pp. 47–50. (2009)

3. Hirose, S., Mori, M.: Biologically inspired snake-like robots. In: 2004 IEEE International Conference on Robotics and Biomimetics, pp. 1–7. (2004)

4. Mori, M., Hirose S.: Three-dimensional serpentine motion and lateral rolling by active cord mechanism ACM-R3. In: IEEE/RSJ International Conference on Intelligent Robots and Systems, vol. 1, pp. 829–834 vol.1. (2002)

5. Tanaka, M., Nakajima, M., Suzuki, Y., Tanaka, K.: Development and control of articulated mobile robot for climbing steep stairs. IEEE/ASME Trans. Mechatron. (99), 1–1 (2018). https://doi.org/10.1109/TMECH.2018.2792013

6. Pfotzer, L., Ruehl, S., Heppner, G., Roennau, A., Dillmann, R.: KAIRO 3: A modular reconfigurable robot for search and rescue field missions. In: 2014 IEEE International Conference on Robotics and Biomimetics (ROBIO 2014), pp. 205–210. (2014)

7. Borenstein, J., Borrell, A.: The OmniTread OT-4 serpentine robot. In: 2008 IEEE International Conference on Robotics and Automation, pp. 1766–1767. (2008)

8. Arai, M., Tanaka, Y., Hirose, S., Kuwahara, H., Tsukui, S.: Development of "Souryu-IV" and "Souryu-V: Serially connected crawler vehicles for in-rubble searching operations. J. Field Robot. **25**, 31–65 (2007). https://doi.org/10.1002/rob.20229

9. Rollinson, D., Bilgen, Y., Brown, B., Enner, F., Ford, S., Layton, C., et al.: Design and architecture of a series elastic snake robot. In: 2014 IEEE/RSJ International Conference on Intelligent Robots and Systems, pp. 4630–4636 (2014)

10. Liljebäck, P., Pettersen, K.Y., Stavdahl, Gravdahl, J.T.: Snake robot locomotion in environments with obstacles. IEEE/ASME Trans. Mechatron. **17**(6), 1158–1169 (2012). https://doi.org/10.1109/TMECH.2011.2159863

11. Vespignani, M., Melo, K., Mutlu, M., Ijspeert, A.J.: Compliant snake robot locomotion on horizontal pipes. In: 2015 IEEE International Symposium on Safety, Security, and Rescue Robotics (SSRR), pp. 1–8. (2015)

12. Takemori, T., Tanaka, M., Matsuno, F.: Gait design for a snake robot by connecting curve segments and experimental demonstration. IEEE Trans. Robot. **34**(5), 1384–1391 (2018)

13. Tsukagoshi, H., Arai, N., Kiryu, I., Kitagawa, A.: Smooth creeping actuator by tip growth movement aiming for search andrescue operation. In: 2011 IEEE International Conference on Robotics and Automation, pp. 1720–1725. (2011)

14. Hawkes, E.W., Blumenschein, L.H, Greer, J.D., Okamura, A.M.: A soft robot that navigates its environment through growth. Sci. Robot. **2**(8), (2017). https://doi.org/10.1126/scirobotics.aan3028. http://robotics.sciencemag.org/content/2/8/eaan3028.full.pdf

15. Coad, M.M., Thomasson, R., Blumenschein, L., Usevitch, N., Hawkes, E.W., Okamura, A.M.: Retraction of soft growing robots without buckling. IEEE Robot. Autom. Lett. 1–1 (2020)

16. Takahashi, T., Tadakuma, K., Watanabe, M., Takane, E., Hookabe, N., Kajiahara, H., et al.: Eversion robotic mechanism with hydraulic skeletonto realize steering function. IEEE Robot. Autom. Lett. **6**(3), 5413–5420 (2021)

17. Isaki, K., Niitsuma, A., Konyo, M., Takemura, F., Tadokoro, S.: Development of an active flexible cable by ciliary vibration drive for scope camera. In: 2006 IEEE/RSJ International Conference on Intelligent Robots and Systems, pp. 3946–3951 (2006)

18. Fukuda, J., Konyo, M., Takeuchi, E., Tadokoro, S.: Remote vertical exploration by active scope camera into collapsed buildings. In: 2014 IEEE/RSJ International Conference on Intelligent Robots and Systems, pp. 1882–1888 (2014)

19. Konyo, M., Isaki, K., Hatazaki, K., Tadokoro, S., Takemura, F.: A ciliary vibration drive mechanism for active scope cameras. J. Robot. Mechatron. **20**(3), 490–499 (2008)

20. Ambe, Y., Yamamoto, T., Kojima, S., Takane, E., Tadakuma, K., Konyo, M., et al.: Use of active scope camera in the kumamoto earthquake to investigate collapsed houses. In: 2016 IEEE International Symposium on Safety, Security, and Rescue Robotics (SSRR), pp. 21–27 (2016)

21. Okada, S., Takai, N.: Classification of structual types and damage patterns of buildings for earthquake field investigation. In: 12th World Conference on Earthquake Engineering (2000)

22. Wright, C, Buchan, A., Brown, B., Geist, J., Schwerin, M., Rollinson, D., et al.: Design and architecture of the unified modular snake robot. In: 2012 IEEE International Conference on Robotics and Automation, pp. 4347–4354 (2012)

23. Ishii, A., Ambe, Y., Yamauchi, Y., Ando, H., Konyo, M., Tadakuma, K., et al.: Design and development of biaxial active nozzle with flexible flow channel for air floating active scope camera. In: 2018 IEEE/RSJ International Conference on Intelligent Robots and Systems (IROS), pp. 442–449 (2018)

24. Fujikawa, T., Yamauchi, Y., Ambe, Y., Konyo, M., Tadakuma, K., Tadokoro, S.: Development of practical air-floating-type active scope camera and user evaluations for urban search and rescue. In: 2019 IEEE International Symposium on Safety, Security, and Rescue Robotics (SSRR), pp. 1–8 (2019)

25. Yamauchi, Y., Ambe, Y., Nagano, H., Konyo, M., Bando, Y., Ito, E., et al.: Development of a continuum robot enhanced with distributed sensors for search and rescue. ROBOMECH J. **9**(8), (2022)

26. Walker, I.D.: Continuous backbone "continuum" robot manipulators. ISRN Robot. **2013**, 726506 (2013)

27. Mehling, J.S, Diftler, M.A., Chu, M., Valvo, M.: A minimally invasive tendril robot for in-space inspection. In: The First IEEE/RAS-EMBS International Conference on Biomedical Robotics and Biomechatronics, 2006. BioRob 2006, pp. 690–695. (2006)

28. Buckingham, R.O., Graham, A.C.: Dexterous manipulators for nuclear inspection and maintenance — Case study. In: 2010 1st International Conference on Applied Robotics for the Power Industry, pp. 1–6. (2010)

29. McMahan, W., Chitrakaran, V., Csencsits, M., Dawson, D., Walker, I.D., Jones, B.A., et al.: Field trials and testing of the OctArm continuum manipulator. In: Proceedings 2006 IEEE International Conference on Robotics and Automation, 2006. ICRA 2006, pp. 2336–2341. (2006)

30. Greer, J.D., Morimoto, T.K., Okamura, A.M., Hawkes, E.W.: Series pneumatic artificial muscles (sPAMs) and application to a soft continuum robot. In: 2017 IEEE International Conference on Robotics and Automation (ICRA), pp. 5503–5510. (2017)

31. Dupont, P.E., Lock, J., Itkowitz, B., Butler, E.: Design and control of concentric-tube robots. IEEE Trans. Robot. **26**(2), 209–225 (2010). https://doi.org/10.1109/TRO.2009.2035740

32. Kiang, C.T., Spowage, A., Yoong, C.K.: Review of control and sensor system of flexible manipulator. J. Intell. Robot. Syst. **77**, 187–213 (2015). https://doi.org/10.1007/s10846-014-0071-4

33. Dehkordi, S.F.: Dynamic analysis of flexible-link manipulator in underwater applications using Gibbs-Appell formulations. Ocean Eng. **241**, 110057 (2021). https://doi.org/10.1016/j.oceaneng.2021.110057

34. Silva Rico, J.A., Endo, G., Hirose, S., Yamada, H.: Development of an actuation system based on water jet propulsion for a slim long-reach robot. ROBOMECH J. **4**(1), 8 (2017). https://doi.org/10.1186/s40648-017-0076-4

35. Campisano, F., Gramuglia, F., Dawson, I.R., Lyne, C.T., Izmaylov, M.L., Misra, S., et al.: Gastric cancer screening in low-income countries: System design, fabrication, and analysis for an ultralow-cost endoscopy procedure. IEEE Robot. Autom. Mag. **24**(2), 73–81 (2017)

36. Campisano, F., Remirez, A.A., Landewee, C.A., Caló, S., Obstein, K.L., Webster, R.J., et al.: Teleoperation and contact detection of a waterjet-actuated soft continuum manipulator for low-cost gastroscopy. IEEE Robot. Autom. Lett. **5**(4), 6427–6434 (2020)

37. Ando, H., Ambe, Y., Ishii, A., Konyo, M., Tadakuma, K., Maruyama, S., et al.: Aerial hose type robot by water jet for fire fighting. IEEE Robot. Autom. Lett. **3**(2), 1128–1135 (2018). https://doi.org/10.1109/LRA.2018.2792701

38. Yamaguchi, T., Ambe, Y., Ando, H., Konyo, M., Tadakuma, K., Maruyama, S., et al.: A mechanical approach to suppress the oscillation of a long continuum robot flying with water jets. IEEE Robot. Autom. Lett. **4**(4), 4346–4353 (2019)

39. Ando, H., Ambe, Y., Yamaguchi, T., Yamauchi, Y., Konyo, M., Tadakuma, K., et al.: Fire extinguishment using a 4?m long flying-hose-type robot with multiple water-jet nozzles. Adv. Robot. **34**(11), 700–714 (2020)

40. Ambe, Y., Yamauchi, Y., Konyo, M., Tadakuma, K., Tadokoro, S.: Stabilized controller for jet actuated cantilevered pipe using damping effect of an internal flowing fluid. IEEE Access **10**, 5238–5249 (2022). https://doi.org/10.1109/ACCESS.2022.3140760

41. Yamauchi, Y., Ambe, Y., Konyo, M., Tadakuma, K., Tadokoro, S.: Realizing large shape deformations of a flying continuum robot with a passive rotating nozzle unit that enlarges jet directions in three-dimensional space. IEEE Access **10**, 37646–37657 (2022). https://doi.org/10.1109/ACCESS.2022.3162835

42. Lee, D.H., Huynh, T., Kim, Y.B., Soumayya, C.: Motion control system design for a flying-type firefighting system with water jet actuators. Actuators **10**(10) (2021)

43. Huynh, T., Lee, D.H., Kim, Y.B.: Study on actuator performance evaluation of aerial water-powered system for firefighting applications. Appl. Sci. **13**(3) (2023). https://doi.org/10.3390/app13031965

44. Mochiyama, H.: Kinematics for the whole arm of a serial-chain manipulator. Adv. Robot. **15**(2), 255–275 (2001). https://doi.org/10.1163/15685530152116263

45. Ariizumi, R., Matsuno, F.: Dynamic analysis of three snake robot gaits. IEEE Trans. Robot. **33**(5), 1075–1087 (2017). https://doi.org/10.1109/TRO.2017.2704581

46. Strogatz, S.H.: Nonlinear dynamics and chaos: with applications to physics, biology, chemistry and engineering. Westview Press (1994)

47. Mohammadi, A., Rezapour, E., Maggiore, M., Pettersen, K.Y.: Maneuvering control of planar snake robots using virtual holonomic constraints. IEEE Trans. Control Syst. Technol. **24**(3), 884–899 (2016). https://doi.org/10.1109/TCST.2015.2467208

48. Yamauchi, Y., Fujimoto, T., Ishii, A., Araki, S., Ambe, Y., Konyo, M., et al.: A robotic thruster that can handle hairy flexible cable of serpentine robots for disaster inspection. In: 2018 IEEE/ASME International Conference on Advanced Intelligent Mechatronics (AIM), pp. 107–113 (2018)

49. Fan, Y., Liu, D., Ye, L.: A novel continuum robot with stiffness variation capability using layer jamming: Design, modeling, and validation. IEEE Access **10**, 130253–130263 (2022). https://doi.org/10.1109/ACCESS.2022.3228775

50. Onda, I., Tadakuma, K., Watanabe, M., Abe, K., Watanabe, T., Konyo, M., et al.: Highly articulated tube mechanism with variable stiffness and shape restoration using a pneumatic actuator. IEEE Robot. Autom. Lett. **7**(2), 3664–3671 (2022). https://doi.org/10.1109/LRA.2022.3147246

Yuichi Ambe received the Ph.D. degree in engineering from Kyoto University, Kyoto, Japan, in 2017. From 2018 to 2022, he was an Assistant Professor at Tohoku University, Japan. Since 2022, he has been an Assistant Professor at the Graduate School of Engineering Science, Osaka University. His research interests include the design and control of jet-actuated continuum robots, legged robots, and rescue robots.

Shuta Kamio received the M.S. degree in information science from Tohoku University, Miyagi, Japan, in 2017. His research interests include the design of jet-actuated continuum robots.

Yu Yamauchi received the Ph.D. degree in Information Science from Tohoku University, Miyagi, Japan, in 2021. Since 2022, he has been an Assistant Professor at the Faculty of Systems Science and Technology, Akita Prefectural University. His research interests include the design and control of continuum robots.

Masashi Konyo received the B.S., M.S., and Ph.D. degrees in engineering from Kobe University, Hyogo, Japan, in 1999, 2001, and 2004, respectively. He is currently an Associate Professor at the Graduate School of Information Sciences, Tohoku University. His research interests include haptic interfaces, rescue robotics, and new actuators. He was a recipient of the Young Scientists Prize, the Commendation for Science and Technology by MEXT in 2015, the Best Paper Awards of the Journals of Robotics and Mechatronics in 2010, Advanced Robotics in 2016, the Best Poster Awards of the IEEE WHC in 2007 and 2013, and Eurohaptics 2018, the Best Demo Awards of Eurohaptics 2008, IEEE Haptics Symposium 2014, and AsiaHaptics in 2018 and 2022.

Kenjiro Tadakuma received the Ph.D. degree in mechanical and aerospace engineering from the Tokyo Institute of Technology, Tokyo, Japan in 2007. He is currently an Associate Professor at the Graduate School of Information Sciences, Tohoku University. His research interests include robotic mechanisms, omnidirectional mobile robots, and rescue robots. Dr. Tadakuma was a recipient of the Young Scientists' Prize for the Commendation of Science and Technology by the Minister of Education, Culture, Sports, Science and Technology (MEXT) in 2011, IEEE ICRA Best Paper Award on Mechanisms and Design in 2019, the Japan Society for the Promotion of Science Prize in 2022. He is the keynote speaker of IROS2022 about "Inventing Robotic Mechanisms."

Shigenao Maruyama received the BS,Ms,and PhD degrees in engineering from Tohoku University in 1977, 1980, 1983, and received the Master of Science from the London University in 1979. He was a professor of Institute of Fluid Science, Tohoku University in 1997–2017, and Distinguished Professor of Tohoku University in 2008–2017. He is president of National Institute of Technology, Hachinohe College in 2017-. He was a member of International Scientific Committee, 3rd International Workshop on Nano-Micro Thermal Radiation (NanoRad) in 2017 and Chair of Board of the Nukiyama Memorial Award 2020, etc. He is the recipients of the Winner of 2015 Elsevier Lightens Your Research Video Contest, Societe Francias De Thermique, 2002 International SFT Award, Award for HTSJ Scientific Contribution, JSME HTD Award for Academic Achievements, JSME Medal for Outstanding Paper, and He is the winner of the Purple Ribbon Medal in 2012. HTSJ Fellow and JSME Fellow.

Satoshi Tadokoro graduated from The University of Tokyo, in 1984. From 1993 to 2005, he was an Associate Professor at Kobe University. Since 2002, he has been the President of the International Rescue System Institute. Since 2005, he has been a Professor at Tohoku University. From 2012 to 2014, he was the Vice/Deputy Dean of the Graduate School of Information Sciences. From 2016 to 2017, he was the President of the IEEE Robotics and Automation Society. Since 2019, he has been the Director of the Tough Cyberphysical AI Research Center, Tohoku University. He served as a Program Manager of the MEXT DDT Project on Rescue Robotics from 2002 to 2007, and was a Project Manager of the Japan Cabinet Office ImPACT Tough Robotics Challenge Project on Disaster Robotics, from 2014 to 2019, with 62 international PIs and 300 researchers who created the Cyber Rescue Canine, Dragon Firefighter, etc. His research team at Tohoku University has developed various rescue robots, of which Quince and Active Scope Camera are widely recognized for their contribution to disaster response, including missions in the Fukushima-Daiichi NPP nuclear reactor buildings. He is an IEEE Fellow, RSJ Fellow, JSME Fellow, and SICE Fellow.